Passivation agent with dipole moment for surface modification towards efficient and stable perovskite solar cells

Ge Wang[a,1], Chen Wang[c,1], Yajun Gao[d], Shanpeng Wen[a,*], Roderick C. I. MacKenzie[e], Liuxing Guo[a], Wei Dong[a], Shengping Ruan[b,*]

[a] College of Electronic Science & Engineering, Jilin University, Changchun 130012, Jilin, China

[b] State Key Laboratory on Integrated Optoelectronics, Jilin University, Changchun 130012, Jilin, China

[c] State Key Laboratory of Supramolecular Structure and Materials, College of Chemistry, Jilin University, Changchun 130012, Jilin, China

[d] KAUST Solar Center (KSC), Physical Sciences and Engineering Division (PSE), King Abdullah University of Science and Technology (KAUST), Thuwal 23955-6900, Kingdom of Saudi Arabia

[e] Faculty of Engineering, The University of Nottingham, University Park, Nottingham, NG7 2RD, UK

[*]Corresponding authors.

Email addresses: sp_wen@jlu.edu.cn (S. Wen), ruansp@jlu.edu.cn (S. Ruan)

[1] These authors contribute equally to this work.

ABSTRACT: Recently, there has been renewed interest in interface engineering as a means to further push the performance of perovskite solar cells closer to the Schockly-Queisser limit. Herein, for the first time we employ a multi-functional 4-chlorobenzoic acid to produce a self-assembled monolayer on a perovskite surface. With this interlayer we observe

passivation of perovskite surface defects and a significant suppression of non-radiative charge recombination. Furthermore, at the surface of the interlayer we observe, charge dipoles which tune the energy level alignment, enabling a larger energetic driving force for hole extraction. The perovskite surface becomes more hydrophilic due to the presence of the interlayer. Consequently, we observe an improvement in open-circuit voltage from 1.08 to 1.16 V, a power conversion efficiency improvement from 18% to 21% and an improved stability under ambient conditions. Our work highlights the potential of SAMs to engineer the photo-electronic properties and stability of perovskite interfaces to achieve high-performance light harvesting devices.

KEYWORDS: 4-chlorobenzoic acid; Interface engineering; Passivation; Surface dipole; Perovskite solar cells

1. Introduction

Perovskite solar cells have attracted intense academic and industrial attention since their conception in 2009. Perovskite devices have demonstrated impressive performances, with power conversion efficiency reaching up to 25% [1] and 28% [2] for single- and tandem-junction cells, respectively. During this period, interface engineering gradually evolved to be an effective strategy to boost device performance and a variety of materials have been successfully employed as interfacial passivation layers [3–7]. Typical examples include Lewis acids or bases, such as fullerene derivatives [8], polymers or organic small molecules with functional group (PMMA, PEO, TOPO etc.) [9–11]. These molecules can passivate under-coordinated trap sites, reduce surface recombination and eliminate the notorious photocurrent hysteresis. Meanwhile, researchers also utilize alkali halides [12], ammonium halide salts [5], zwitterions [13], aiming to form ionic bonding, so as to passivate multiple ionic defects on the surface such as PbI^{3-}, Pb^{2+}, MA^{+} vacancies. In addition to passivation based on molecular interaction, a 2D layered phase has recently been used to chemically convert surface defects to an extended structural layer and thus achieve high-electronic-quality perovskite films [14]. All of these findings have showcased the potential of passivation layers to optimize the performance of novel perovskite cells.

Researchers have further realized that an optimum interlayer should boost not only electrical efficiency, but also stability and lifetime concurrently. From the electrical perspective, the layer should neutralize defects, optimize interface band alignment and have a low series resistance [15] to optimized for both recombination and extraction of carriers [16]. Furthermore, to reduce moisture-induced degradation and extend the life span of devices the interlayer should be hydrophobic [17]. Considering, the complex and often contradictory requirements of these multi-functional passivation layers, self-assembled monolayers (SAMs) of organic molecules provide a flexible platform onto which to build. By integrating different

functional groups, SAMs can be tailored to match the multifaceted requirements. SAMs have already seen extensive application in other fields [18–22], such as organic solar cells, light-emitting diodes and detectors. It was reported by Wang et.al that the application of phenylalkylamine SAM molecules can suppress open-circuit voltage (V_{oc}) deficit to under 0.36 V (this is widely regarded as one the most important achievements for perovskite solar cells) [23]. In the meantime, by anchoring perfluorinated SAMs onto perovskites, Dieter et al. not only significantly improved the performance but also improve device stability [24]. These relatively few but important findings point to a bright future for SAM materials to be used as surface passivation layers in perovskite cells. Previous work done with 4-chlorobenzoic acid (4-ClBA) has demonstrated it can modify the transport layer on the front of the device. Jen et al. modified a NiO_x layer with 4-ClBA which passivated the surface defects and improved the interfacial energy alignment [25]. Pauporté et al. introduced 4-ClBA between TiO_2 and perovskite, which facilitated electron transfer from perovskite to TiO_2 due to increased structural continuity between two layers [26]. 4-ClBA also been shown to improve the crystalline quality of perovskite layer. Additionally, Jin et al. reported a 4-ClBA doped TiO_2 layer, which showed improved electron mobility, and thus enhanced device performance [27]. However, as of yet, there has been no report modifying the perovskite surface with a 4-ClBA SAM layer.

In this work, we report that the SAM of 4-chlorobenzoic acid (4-ClBA) anchors onto $MAPbI_3$ perovskite layer (Fig. 1a). By bonding with uncoordinated lead defects on perovskite surface, 4-ClBA reduced the density of trap states and thus reduced non-radiative charge recombination. Meanwhile, the bonding between SAMs and defects in turn introduces a dipole layer with favorable orientation on perovskite surface, which down-shifts the valance band of perovskite thus increases perovskite/spiro-OMeTAD energy offset for charge extraction through the interface. These are confirmed by significantly enhanced V_{oc} and fill

factor (*FF*) of passivated device and is substantiated by spectroscopy and charge transport/recombination dynamics study. Consequently, the champion device with 4-ClBA passivation demonstrates a promising power conversion efficiency (PCE) up to 21% with negligible hysteresis. The device also exhibits enhanced ambient stability, which maintains 80% of the initial efficiency after aging a month under ambient atmosphere (50%±5% RH, 25 degrees centigrade) without encapsulation. This work shows that multi-functional SAM passivators are a promising avenue to reach high-stability perovskite devices.

2. Results and discussion

We fabricate perovskite solar cells using the n-i-p planar configuration. The $MAPbI_3$ perovskite is synthesized through one-step anti-solvent method and sandwiched between electron transport layer SnO_2 and hole transport layer Spiro-OMeTAD. As the earliest developed perovskite light absorber, $MAPbI_3$ enables good device-to-device reprehensibility and countable categories of defects [28]. Homogeneous and pinhole-free perovskite film were obtained with the average grain size around 400 nm. X-ray diffraction (XRD) peaks corresponding to (110) and (220) indicate the cubic perovskite phase (Fig. S1) [29]. For the 4-ClBA treatment, 4-ClBA solution in anhydrous isopropanol was spin-coated onto $MAPbI_3$ followed by baking at 100 °C for 5 min. We observe no difference in morphology or crystallization of the perovskite after covering with 4-ClBA, as indicated by scanning electron microscopy (SEM), atomic force microscopy (AFM) and XRD tests (Fig. S2). This can be attributed to the relatively low 4-ClBA concentration (1 mg/mL). In order to confirm the existence of 4-ClBA on the perovskite surface, X-ray photoelectron spectra (XPS) measurements are performed, as shown in Fig. 1(b) (see full spectra in Fig. S3). The occurrence of an asymmetric peak at around 202 eV in 4-ClBA group, which can be deconvoluted into two peaks located at 201.4 and 203.3 eV. This coincides with Cl 2p3/2 and2p1/2 core level thus confirms the existence of 4-ClBA at the perovskite surface [30]. We

speculate the deposited 4-ClBA is very thin or may even be a mono layer as that they cannot be distinguished from SEM and AFM measurements. Fig. S4 shows that the 4-ClBA is insoluble in chlorobenzene solvent, which confirms it won't be affected after spin-coating Spiro-OMeTAD layer. More evidence of 4-ClBA SEM existence comes from the water contact angle measurement. As shown by Fig. 1(c), it is clear that the pristine perovskite exhibits a small angle of 20°, while perovskite treated by 4-ClBA displays increased contact angle of 63°. Hence, it is reasonable to conclude that the covered 4-ClBA makes the perovskite surface less hydrophilic due to its water-resistive organic moiety [23,24,31,32]. The XRD tests on aged perovskite films with and without 4-ClBA were conducted to check the film stability. The films are exposed to 50%±5% RH without encapsulation at room temperature under dark conditions. Fig. 1(d and e) shows the initial state and after 28 days of the tested films, respectively. It can be seen that the pristine perovskite film undergoes severe decomposition as also confirmed by the XRD pattern. While 4-ClBA treatment significantly inhibits film decomposition with obvious color change only at the edges. The better stability can be attributed to the fact that 4-ClBA reduces hydrophilicity of perovskite film. Ultraviolet photoelectron spectroscopy (UPS) measurements were performed to investigate the energy alignment change due to 4-ClBA modification. The Fermi energy level (E_f) is extracted from secondary electron cut-off edge of the UPS spectrum in Fig. 1(f) (hv = 21.22 eV). The calculated E_f of perovskite before and after 4-ClBA modification is −4.04 and −4.22 eV, respectively. In the valence region, the onset edge is 1.33 and 1.28 eV for the pristine perovskite and perovskite/4-ClBA, respectively. Therefore, the valence band maximum (VBM) can be calculated as −5.37 and −5.50 eV. The Tauc plot (Fig. S5) of perovskite and 4-ClBA-treated perovskite reveals bandgaps of 1.60 eV [33,34], from which can be also determined from the conduction band minimum. The energy structure of entire device is summarized in Fig. 1(g). The upshift in vacuum level with the assembled 4-ClBA suggests

the formation of a dipole interlayer with the positive end pointed towards perovskite and the negative end pointed away from it [35]. This is also consistent with the fact that 4-ClBA sets up a surface dipole with $D>0$, leading to the increased work function [36]. Moreover, the 4-ClBA molecule has been broadly used in optoelectronic devices. An orderly assembled 4-ClBA SAM would set up a surface dipole that provides the high work function [25,37]. While a layer with randomly orientated 4-ClBA molecules would lead to no interfacial dipole. Here the dipole effect is confirmed by surface work function change of perovskite from 4.04 to 4.22 eV after modification, also indicating that to some extent 4-ClBA molecules are self-assembled on the perovskite. Moreover, downshifting VBM by 0.13 eV was achieved after the 4-ClBA modification, which is expected to be beneficial for increasing the energetic driving force for charge extraction and thus suppress interfacial recombination [38]. The deeper conduction band minimum the larger barrier, which will block electron flow [39].

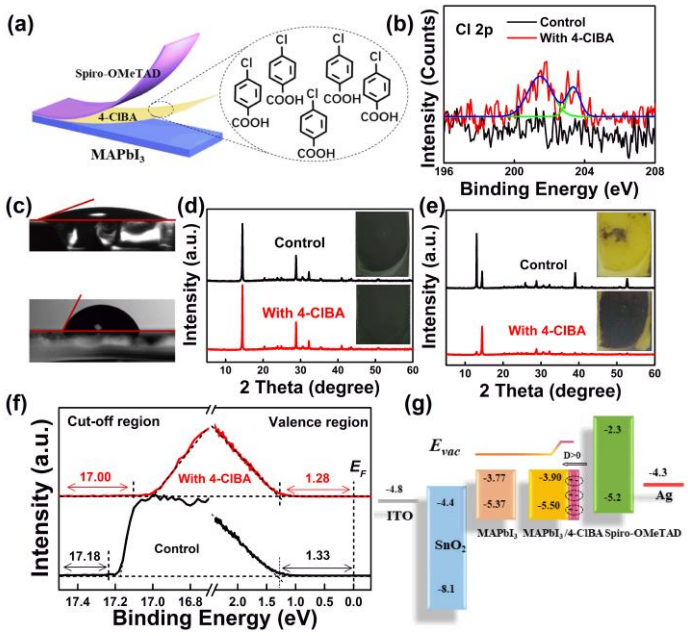

Fig. 1. (a) A schematic diagram of the chemical structure and orientation of 4-ClBA molecules on the perovskite film. (b) The fine XPS spectra of Cl 2p core level in 4-ClBA. (c) Water droplet contact angles on perovskite films with and without 4-ClBA. The XRD and film decomposition profiles of perovskite with and without 4-ClBA (d) at the initial state and (e) after 28 days. (f) The UPS spectra and (g) the energy level diagram of perovskite with and without 4-ClBA.

To understand how 4-ClBA interacts with the perovskite surface thus passivates the defects states, we employ Fourier transform infrared spectroscopy (FTIR) and XPS analyses. Fig. 2(a) shows the FTIR spectra of 4-ClBA film deposited on $MAPbI_3$ film (on KBr plate) and bare KBr plate. Before measurement, the bare KBr plate is tested as a background. We observe the characteristic peak representing the C=O stretch vibration bond of carboxyl on 4-ClBA molecule located at 1680 cm^{-1} [40]. This peak shifts to lower wavenumbers from 1680 to 1666 cm^{-1} when 4-ClBA film is deposited on perovskite. This implies a decreased bond energy, resulting from the deviation of the electronic cloud of C=O away from 4-ClBA molecule after bonding with the perovskite surface. Considering the defects in $MAPbI_3$, we conjecture that coordination between oxygen atoms of carboxyl group and uncoordinated lead defects of perovskite occurs, which has previously been reported by others [41–43]. Further evidence is obtained from XPS analysis. We first use the carbon 1 s line (for hydrocarbons or hydrocarbon-containing groups) to calibrate the binding-energy scale. Fig. 2(b) displays the Pb 4f core level, which shows the Pb 4f7/2 and 4f5/2 peaks of the pristine $MAPbI_3$ centered at 138.6 and 143.4 eV, respectively. After being modified with 4-ClBA, the Pb 4f peaks shift toward lower binding energies to 138.4 and 143.2 eV, respectively. The lower binding energy indicates that the surface uncoordinated lead site is passivated by the carboxyl of 4-ClBA molecule [43–45], which is in line with FTIR result. Meanwhile, the 3d peak of I, as shown in Fig. 2(c), also downward shifts about 0.3 eV after 4-ClBA

modification. A change in the electronic doping level, and thus in Fermi level position, should lead to a shift of the core level positions. In this case, both the Pb and I core level spectra shift by 0.2 and 0.3 eV toward lower binding energy for the 4-ClBA-treated perovskite as compared to the control sample, indicative of a shift of interfacial electronic states towards p-type [46,47], this is also consistent with the UPS results. As is well known, the interfacial electronic states play an important role in charge carrier dynamics at interfaces. It has been demonstrated that perovskite deposited on electron transport layers (such as SnO_2 or TiO_2) exhibit n-type electronic states [48], which are not conducive to hole extraction on the Spiro-OMeTAD side. 4-ClBA modification contributes to the perovskite surface with weakened n-type doping. This is more compatible with the n-i-p configuration, guaranteeing an enhanced hole extraction by Spiro-OMeTAD hole transport layer.

Steady state (PL) and time-resolved photoluminescence (TRPL) measurements were conducted to further confirm the passivation efficacy derived from 4-ClBA and investigate the charge dynamic of the device. Fig. 2(d) shows the PL spectra of pristine and 4-ClBA modified perovskite on glass excited by 405 nm light. As shown in the curves plotted with spheres, the PL peak located at 765 nm and its intensity after 4-ClBA modification is around 1.5 times that of control sample. This implies a less non-radiative charge recombination associated with lower density of perovskite traps after 4-ClBA treatment. The corresponding PL lifetime of perovskite film are shown in Fig. 2(e) (curve with sphere). The TRPL curves were fitted into biexponential decay $Y=Y_0+f_1\exp(-(t-t_0)/\tau_1) + f_2\exp(-(t-t_0)/\tau_2)$, with detailed fitting parameters are summarized in Table S1. It has been demonstrated that the τ_1 part is related to the trapping process or trap-assisted charge recombination and the τ_2 part is related to the detrapping process or radiative charge recombination [49–51]. Upon 4-ClBA modification, we observe decreased portion of fast decay process (f_1 from 11.89% to 7.59%) and increased τ_1 from 7.08 to 11.87 ns, indicating the charge trapping or trap-assisted

recombination is inhibited and the PL decay is more dominated by radiative charge recombination process. The increased τ_2 from 98.66 to 145.24 ns also suggests suppressed trap-assisted recombination [52]. After 4-ClBA modification, the hole extraction efficiency through the perovskite/Spiro-OMeTAD interface was also investigated in glass/perovskite/spiro-OMeTAD geometry. As shown in curves with circle in Fig. 2(d), the calculated PL quenching efficiency of perovskite/4-ClBA/Spiro-OMeTAD exceeds 90% while only 70.5% for perovskite/Spiro-OMeTAD. A faster PL decay profile is also observed in Fig. 2(e) (red curve with circles) in the 4-ClBA case. These results demonstrate a better hole extraction with 4-ClBA treatment [7,53–55]. This improved hole extraction could originate from the enlarged energetic driving force and reduced perovskite surface defects by 4-ClBA passivation, and would likely lead to enhanced photovoltaic performance.

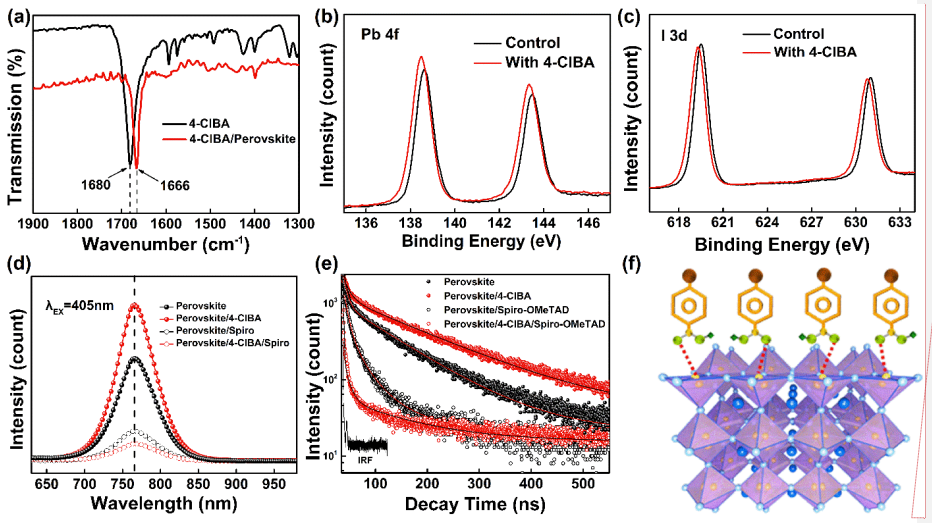

Commented [g1]: (c) x-axis title should be fully displayed the unit counts should be count

Fig. 2. (a) FTIR transmission spectra of pristine 4-ClBA and 4-ClBA on perovskite. XPS spectra of (b) Pb 4f and (c) I 3d core-level of $MAPbI_3$ with and without 4-ClBA. (d) The steady state PL of perovskite and perovskite/spiro-OMeTAD film with and without 4-ClBA modification. (e) The time-resolved PL of perovskite and perovskite/spiro-OMeTAD film with and without 4-ClBA modification (the excitation laser pulse is at 485 nm and ~8

nJ/cm^2), IRF is the response function of equipment. (f) The schematic of the bonding interaction between perovskite and 4-ClBA.

In order to investigate the influence of the 4-ClBA modification on photovoltaic performance, we fabricated planar heterojunction perovskite devices with the structure ITO/SnO_2/perovskite/without or with 4-ClBA/Spiro-OMeTAD/Ag. Fig. 3(a) shows the cross-sectional SEM images, a well-defined layer-by-layer structure with sharp interfaces can be observed. We first perform a series of experiments to optimize the concentration of 4-ClBA solution. The dependence of the device performance on the 4-ClBA deposition concentration is described in Fig. S6 in supporting information. The detail parameters are summarized in Table S2. The highest PCE is obtained at 1 mg/mL 4-ClBA concentration and this concentration is adopted throughout the experiments. Devices based on $MAPbI_3$ without 4-ClBA modification are fabricated as the control group. Current density-voltage (*J*-*V*) curves measured from under AM 1.5 G illumination are shown in Fig. 3(b), with the detail parameters of the best device are listed in Table 1. The control device gives a reverse scanning efficiency of 17.98% with a V_{oc} of 1.08 V, short-circuit current density (J_{sc}) of 22.63 mA/cm^2 and fill factor of 0.74. By contrast, 4-ClBA modified devices show a significantly higher V_{oc} of 1.16 V and fill factor of 0.79, demonstrating a lower voltage loss of 0.41 V (bandgap derived from IPCE spectrum) and champion PCE of 21%. The improved performance can be attributed to the suppressed non-radiative recombination and better charge extraction within 4-ClBA based device. Moreover, the optimized device shows a reduced photocurrent hysteresis (hysteresis factor of 0.032) compared with the control device (hysteresis factor of 0.208). This can be attributed to the reduced surface charge recombination, which is considered to be origin of photocurrent hysteresis of perovskite cells [8]. The incident photon-to-electron conversion efficiency (IPCE) measurements are conducted to check the reliability of *J*-*V* measurement. As shown in Fig. 3(c), the integrated

current density calculated from the IPCE spectrum is 22.86 and 22.42 mA/cm^2, respectively, this agrees with the *J-V* measurements. To get a more comprehensive evaluation of influence of 4-ClBA on device performance, we repeatedly fabricate 20 individual devices of two types. Fig. 3(d) shows the efficiency distribution histogram, which indicates 4-ClBA modified devices present more concentrated and higher PCE distribution than the control devices, confirming improved performance and reproducibility. The steady-state photocurrent and power output tracking at the maximum power point for 150 s are depicted in Fig. 3(e). The control and 4-ClBA modified device deliver stable current density of 19.19, 20.88 mA/cm^2 and stable efficiency of 15.87%, 19.95%, respectively. Fig. 3(f) compares the long-term stability of two type devices under ambient atmosphere (50%±5% RH, 25 degrees centigrade) without encapsulation. The 4-ClBA modified device is much more stable, maintaining 80% of the initial PCE after around 700 hours while the control device loses over 50% of its efficiency after 200 h. This is consistent with the improved intrinsic stability of 4-ClBA modified perovskite film.

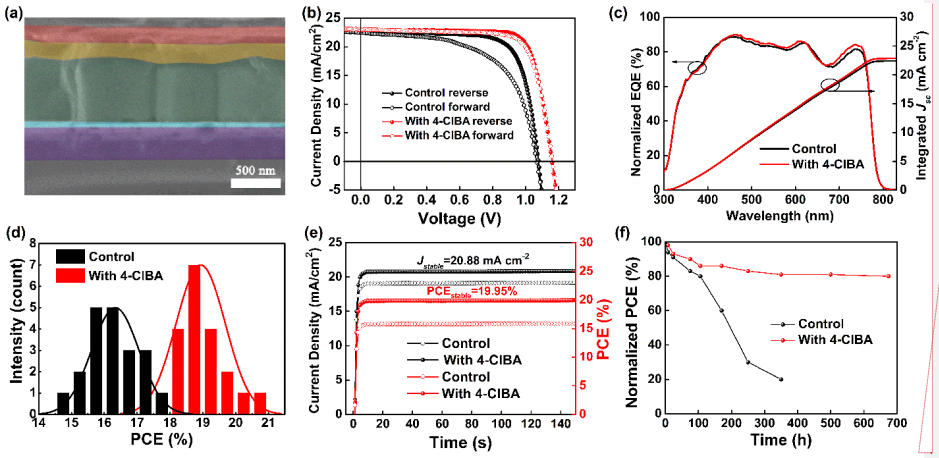

Fig. 3. (a) A cross-section SEM image of the perovskite device. (b) *J-V* curves of cells based on $MAPbI_3$ with and without 4-ClBA modification in different scan directions. (c) Corresponding IPCE and integrated J_{sc} of devices. (d) Statistical PCE distribution for devices

Commented [g2]: counts should be count

reported within this paper. (e) Maximal steady-state photocurrent output tracking at the maximum power point under continuous testing. (f) Devices stability test under ambient atmosphere (50%±5% RH, 25 degrees centigrade) without encapsulation.

Table 1. Photovoltaic parameters of PSCs based on $MAPbI_3$ with and without 4-ClBA coating.

		J_{sc} (mA/cm^2)	V_{oc} (V)	FF	PCE (%)	Hysteresis factor
Modified device	forward	22.64±0.25	1.14±0.01	0.73±0.02	19.02±0.64 (20.31)	0.032
	reverse	22.76±0.18	1.15±0.01	0.74±0.03	19.18±0.72 (20.99)	
Control device	forward	22.07±0.37	1.05±0.01	0.62±0.03	14.49±0.59 (14.24)	0.208
	reverse	22.15±0.39	1.07±0.01	0.70±0.02	16.36±0.74 (17.98)	

*Values in the brackets are in consistent with the *J-V* curves of Fig. 3(b).

We further investigate influences of 4-ClBA treatment on charge recombination and charge extraction processes. To do this we perform transient photovoltage (TPV) and transient photocurrent (TPC) measurements. In TPV, the device is exposed in a background light under open-circuit condition, which generates photovoltage approximate to V_{oc}. Then an attenuated green laser pulse is used to produce a small voltage perturbation (ΔV) of 50 mV. The decay rate of the voltage increment transient can be used to probe the charge recombination lifetime, as shown in Fig. 4(a). We fit the TPV curves using mono-exponential decay by the equation [56]:

$$\Delta V(t) = \Delta V_0 e^{-\frac{t}{\tau_{\Delta n}}} \quad (1)$$

The charge lifetime increases from 9.9 μs in control case to 13.8 μs after 4-ClBA treatment, indicating a reduced charge recombination. Fig. 4(b) shows the TPC transient, which allows us to evaluate the charge extraction process. The fitted charge extraction time (via mono-exponential decay) is reduced from 0.97 μs for control device to 0.48 μs for 4-ClBA based device. This further confirms the enhanced charge extraction due to the engineered band alignment and surface passivation by 4-ClBA treatment.

Next we use space charge limited current (SCLC) and thermal admittance spectroscopy (TAS) techniques to get more quantitative information about how 4-ClBA treatment affects trap states. Fig. 4(c) shows the dark *J-V* curve of hole-only device (structured with ITO/PEDOT:PSS/perovskite/spiro-OMeTAD/Ag), which is divided into three regions according to different slopes (*n*). The resistance region, i.e., *n*=1, in which current is linearly dependent to voltage. Then the curve enters to trap-filling region (starts at V_{TFL}) where the current shows a rapid nonlinear rise (*n*>3). When all traps states are filled by the injected carriers signaled transition into space charge limited region (*n*=2). The trap density can be calculated through the equation [14,57,58]:

$$2\varepsilon\varepsilon_0 V_{TFL} = eN_{trap}L^2, \qquad (2)$$

where V_{TFL} is trap filled limit voltage, L is the thickness of the $MAPbI_3$ layer, ε is the relative dielectric constant of $MAPbI_3$ (ε=32), and ε_0 is the vacuum permittivity. It can be calculated that the trap density decreased from 5.09×10^{15} cm^{-3} to 2.43×10^{15} cm^{-3} after the modification with 4-ClBA. We further calculated the carrier mobility from the SCLC measurement. The dark *J-V* characteristic was plotted into a semi-log scale, as shown in Fig. S7 and fitted according to the equation [59]:

$$J(V) = \frac{9}{8}\varepsilon\varepsilon_0\mu\exp\left(0.89\beta\sqrt{\frac{V-V_{bi}}{L}}\right)\frac{(V-V_{bi})^2}{L^3} \qquad (3)$$

The hole mobility is 6.14×10^{-5} $cm^2/(V\ s)$ and 8.54×10^{-4} $cm^2/(V\ s)$ for control and 4-ClBA optimized device, respectively. It can be seen that compared to the pristine perovskite film, the charge transport in the 4-ClBA treated film is significantly enhanced. The hole mobility is 1 order of magnitude larger than the control film. The increased mobility contributes to higher FF and efficiency of the device, which is consistent to the previous discussion. The TAS is a well-established technique to characterize the trap density of states (tDOS) and energetic distribution over the whole trap depth region [6–8,13]. Fig. 4(d) shows the tDOS of

control and 4-ClBA optimized device, which is calculated from capacitance versus voltage (*C*–*V*) and capacitance versus frequency (*C*–*F*) curves of corresponding devices (Fig. S8). We can see that the tDOS decreases about one order of magnitude after the 4-ClBA modification. And the difference is more significant in E_ω region of 0.45–0.52 eV. It can be inferred that the 4-ClBA SAM effectively passivates traps in relative deep levels, which are mainly assigned to be defects at the film surface and responsible for the non-radiative recombination centers [8,13]. The above results quantitatively support the passivation efficacy from 4-ClBA modification.

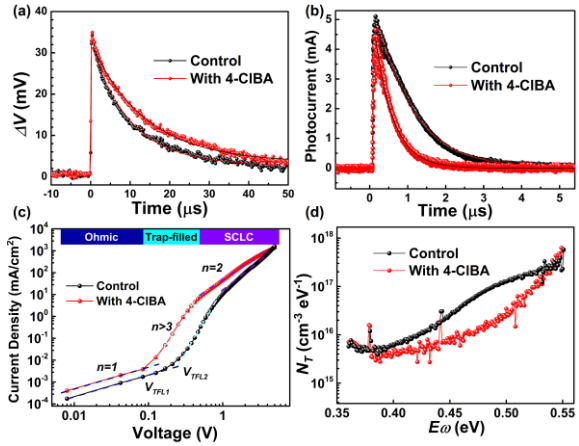

Fig. 4. (a) Transient photovoltage decay and (b) raw data of transient photocurrent decay of the devices features on $MAPbI_3$ with and without 4-ClBA modification. (c) *J*-*V* curves of the hole-only device. (d) The tDOS comparison of the two devices obtained by thermal admittance spectroscopy.

3. Conclusions

In summary, we demonstrate that a 4-ClBA SAM can be used as a multi-function surface passivation layer of perovskite solar cells. Under-coordinated lead-related defects are effectively passivated after bonding with the carboxyl group of 4-ClBA. This inhibits the

non-radiative recombination losses and helps to improve V_{oc} from 1.08 to 1.16 V. Meanwhile, 4-ClBA SAM also introduces an additional surface dipole as a result of the regular orientation, with carboxyl group pointing towards perovskite and organic moiety pointing towards charge extraction layer. The surface dipole alters the band alignment by lowering the valence band of perovskite and thus contributes to the charge extraction. Moreover, the organic moiety renders the perovskite more hydrophobic, so the cells become more resilient against moisture-induced degradation. Finally, all of these results combined enable us to improve push the performance as high as 21%, eliminate the hysteresis, and extend the lifespan of the devices. These findings point to the future potential of multi-functional SAMs as an effective passivation layer of perovskite solar cells.

Supporting Information

Device fabrication process; XRD spectra, AFM, SEM, full spectra of XPS, absorption spectrum and Tauc plot of the $MAPbI_3$ films with and without 4-ClBA; *J-V* curves and table of photovoltaic parameters of devices dependent on different 4-ClBA concentrations; C-V and C-F dependence curves based on modified and control device; table of fitting parameters of TRPL decay.

Declaration of Competing Interest

The authors declare no competing financial interest.

Acknowledgments

This work was supported by the National Natural Science Foundation of China (Grant Nos. 52073115, 61874048, 12073009), the Project of Science and Technology Development Plan of Jilin Province (Grant No. 20200201085JC).

References

[1] https://www.nrel.gov/pv/cell-efficiency.html, accessed at 2021.2.25.

[2]https://www.oxfordpv.com/news/oxford-pv-perovskite-solar-cell-achieves-28-efficiency, accessed at 2021.2.25.

[3] H. Tan, A. Jain, O. Voznyy, X. Lan, F.P. García de Arquer, J.Z. Fan, R. Quintero-Bermudez, M. Yuan, B. Zhang, Y. Zhao, F. Fan, P. Li, L.N. Quan, Y. Zhao, Z.-H. Lu, Z. Yang, S. Hoogland, E.H. Sargent, Science 355 (2017) 722-726.

[4] E.A. Alharbi, A.Y. Alyamani, D.J. Kubicki, A.R. Uhl, B.J. Walder, A.Q. Alanazi, J. Luo, A. Burgos-Caminal, A. Albadri, H. Albrithen, M.H. Alotaibi, J.E. Moser, S.M. Zakeeruddin, F. Giordano, L. Emsley, M. Gratzel, Nat. Commun. 10 (2019) 3008, 1-9.

[5] Q. Jiang, Y. Zhao, X. Zhang, X. Yang, Y. Chen, Z. Chu, Q. Ye, X. Li, Z. Yin, J. You, Nat. Photonics 13 (2019) 460-466.

[6] S. Yang, S. Chen, E. Mosconi, Y. Fang, X. Xiao, C. Wang, Y. Zhou, Z. Yu, J. Zhao, Y. Gao, F. De Angelis, J. Huang, Science 365 (2019) 473-478.

[7] R. Wang, J. Xue, K.-L. Wang, Z.-K. Wang, Y. Luo, D. Fenning, G. Xu, S. Nuryyeva, T. Huang, Y. Zhao, J.L. Yang, J. Zhu, M. Wang, S. Tan, I. Yavuz, K.N. Houk, Y. Yang, Science 366 (2019) 1509-1513.

[8] Y. Shao, Z. Xiao, C. Bi, Y. Yuan, J. Huang, Nat. Commun. 5 (2014) 5784, 1-7.

[9] D. Bi, C. Yi, J. Luo, J.-D. Décoppet, F. Zhang, Shaik M. Zakeeruddin, X. Li, A. Hagfeldt, M. Grätzel, Nat. Energy 1 (2016) 1-5.

[10] Z. Wu, Z. Liu, Z. Hu, Z. Hawash, L. Qiu, Y. Jiang, L.K. Ono, Y. Qi, Adv. Mater. 31 (2019) 1804284, 1-7.

[11] I.L. Braly, D.W. deQuilettes, L.M. Pazos-Outón, S. Burke, M.E. Ziffer, D.S. Ginger, H.W. Hillhouse, Nat. Photonics 12 (2018) 355-361.

[12] M. Abdi-Jalebi, Z. Andaji-Garmaroudi, S. Cacovich, C. Stavrakas, B. Philippe, J.M. Richter, M. Alsari, E.P. Booker, E.M. Hutter, A.J. Pearson, S. Lilliu, T.J. Savenije, H. Rensmo, G. Divitini, C. Ducati, R.H. Friend, S.D. Stranks, Nature 555 (2018) 497-501.

[13] X. Zheng, B. Chen, J. Dai, Y. Fang, Y. Bai, Y. Lin, H. Wei, X. Zeng, J. Huang, Nat. Energy 2 (2017) 1-9.

[14] J. Zhuang, P. Mao, Y. Luan, X. Yi, Z. Tu, Y. Zhang, Y. Yi, Y. Wei, N. Chen, T. Lin, F. Wang, C. Li, J. Wang, ACS Energy Lett. 4 (2019) 2913-2921.

[15] M. Stolterfoht, P. Caprioglio, C.M. Wolff, J.A. Márquez, J. Nordmann, S. Zhang, D. Rothhardt, U. Hörmann, Y. Amir, A. Redinger, L. Kegelmann, F. Zu, S. Albrecht, N. Koch, T. Kirchartz, M. Saliba, T. Unold, D. Neher, Energy Environ. Sci. 12 (2019) 2778-2788.

[16] A. Fakharuddin, L. Schmidt-Mende, G. Garcia-Belmonte, R. Jose, I. Mora-Sero, Adv. Energy Mater. 7 (2017) 1700623, 1-44.

[17] Y. Bai, Q. Dong, Y. Shao, Y. Deng, Q. Wang, L. Shen, D. Wang, W. Wei, J. Huang, Nat. Commun. 7 (2016) 12806, 1-9.

[18] G. Ligorio, G.F. Cotella, A. Bonasera, N. Zorn Morales, G. Carnicella, B. Kobin, Q. Wang, N. Koch, S. Hecht, E.J.W. List-Kratochvil, F. Cacialli, Nanoscale 12 (2020) 5444-5451.

[19] Y. Lin, Y. Firdaus, F.H. Isikgor, M.I. Nugraha, E. Yengel, G.T. Harrison, R. Hallani, A. El-Labban, H. Faber, C. Ma, X. Zheng, A. Subbiah, C.T. Howells, O.M. Bakr, I.

Commented [g3]: page numbers

McCulloch, S.D. Wolf, L. Tsetseris, T.D. Anthopoulos, ACS Energy Lett. 5 (2020) 2935-2944.

[20] G. Yang, C. Wang, H. Lei, X. Zheng, P. Qin, L. Xiong, X. Zhao, Y. Yan, G. Fang, J. Mater. Chem. A 5 (2017) 1658-1666.

[21] L. Zuo, Q. Chen, N. De Marco, Y.T. Hsieh, H. Chen, P. Sun, S.Y. Chang, H. Zhao, S. Dong, Y. Yang, Nano Lett. 17 (2017) 269-275.

[22] S.Y. Kim, S.J. Cho, S.E. Byeon, X. He, H.J. Yoon, Adv. Energy Mater. 10 (2020) 2002606, 1-26.

[23] F. Wang, W. Geng, Y. Zhou, H.H. Fang, C.J. Tong, M.A. Loi, L.M. Liu, N. Zhao, Adv. Mater. 28 (2016) 9986-9992.

[24] C.M. Wolff, L. Canil, C. Rehermann, N. Ngoc Linh, F. Zu, M. Ralaiarisoa, P. Caprioglio, L. Fiedler, M. Stolterfoht, S. Kogikoski, Jr., I. Bald, N. Koch, E.L. Unger, T. Dittrich, A. Abate, D. Neher, ACS Nano 14 (2020) 1445-1456.

[25] Q. Wang, C.C. Chueh, T. Zhao, J. Cheng, M. Eslamian, W.C.H. Choy, A.K. Jen, ChemSusChem 10 (2017) 3794-3803.

[26] T. Zhu, J. Su, F. Labat, I. Ciofini, T. Pauporte, ACS Appl. Mater. Interfaces 12 (2020) 744-752.

[27] V.M. Arivunithi, S. Kim, J. Choi, J.H. Sung, H.D. Yoo, E.-S. Shin, Y.-Y. Noh, Y.-S. Gal, H. Lee, S.-H. Jin, Organic Electronics, 86 (2020) 105922, 1-8.

[28] L. Fu, H. Li, L. Wang, R. Yin, B. Li, L. Yin, Energy Environ. Sci., 13 (2020) 4017-4056.

Commented [g4]: please check all the following references carefully

[29] Y. Li, L. Meng, Y.M. Yang, G. Xu, Z. Hong, Q. Chen, J. You, G. Li, Y. Yang, Y. Li, Nat Commun, 7 (2016) 10214, 1-10.

[30] J. Chen, X. Zhao, S.G. Kim, N.G. Park, Adv. Mater., 31 (2019) 1902902, 1-10.

[31] X. Zheng, J. Troughton, N. Gasparini, Y. Lin, M. Wei, Y. Hou, J. Liu, K. Song, Z. Chen, C. Yang, B. Turedi, A.Y. Alsalloum, J. Pan, J. Chen, A.A. Zhumekenov, T.D. Anthopoulos, Y. Han, D. Baran, O.F. Mohammed, E.H. Sargent, O.M. Bakr, Joule, 3 (2019) 1963-1976.

[32] Z. Yang, J. Dou, S. Kou, J. Dang, Y. Ji, G. Yang, W.Q. Wu, D.B. Kuang, M. Wang, Adv. Funct. Mater., 30 (2020) 1910710, 1-9.

[33] F. Li, Y. Xie, Y. Hu, M. Long, Y. Zhang, J. Xu, M. Qin, X. Lu, M. Liu, ACS Energy Lett., 5 (2020) 1422-1429.

[34] D. Chi, S. Huang, M. Zhang, S. Mu, Y. Zhao, Y. Chen, J. You, Advanced Functional Mater., 28 (2018) 1804603, 1-6.

[35] M. Zhang, Q. Chen, R. Xue, Y. Zhan, C. Wang, J. Lai, J. Yang, H. Lin, J. Yao, Y. Li, L. Chen, Y. Li, Nat Commun, 10 (2019) 4593, 1-9.

[36] T.C. Leung, C.L. Kao, W.S. Su, Y.J. Feng, C.T. Chan, Phy. Rev. B, 68 (2003) 195408, 1-5.

[37] H. Choi, H.B. Kim, S.J. Ko, J.Y. Kim, A.J. Heeger, Adv. Mater., 27 (2015) 892-896.

[38] S. Ryu, J.H. Noh, N.J. Jeon, Y. Chan Kim, W.S. Yang, J. Seo, S.I. Seok, Energy Environ. Sci., 7 (2014) 2614-2618.

[39] H.-J. Jhuo, P.-N. Yeh, S.-H. Liao, Y.-L. Li, S. Sharma, S.-A. Chen, J. Mater. Chem. A, 3 (2015) 9291-9297.

[40] https://spectrabase.com/spectrum/JAnlbSPZIgB, access at 2021.2.25.

[41] X. Li, C.-C. Chen, M. Cai, X. Hua, F. Xie, X. Liu, J. Hua, Y.-T. Long, H. Tian, L. Han, Adv. Energy Mater., 8 (2018) 1800715, 1-7.

[42] K. Chen, J. Wu, Y. Wang, Q. Guo, Q. Chen, T. Cao, X. Guo, Y. Zhou, N. Chen, M. Zhang, Y. Li, J. Mater. Chem. A, 7 (2019) 21140-21148.

[43] Z. Liu, F. Cao, M. Wang, M. Wang, L. Li, Angew. Chem. Int. Ed. Engl., 59 (2020) 4161-4167.

[44] N.K. Noel, S.N. Habisreutinger, A. Pellaroque, F. Pulvirenti, B. Wenger, F. Zhang, Y.-H. Lin, O.G. Reid, J. Leisen, Y. Zhang, S. Barlow, S.R. Marder, A. Kahn, H.J. Snaith, C.B. Arnold, B.P. Rand, Energy Environ. Sci., 12 (2019) 3063-3073.

[45] X. Zhu, M. Du, J. Feng, H. Wang, Z. Xu, L. Wang, S. Zuo, C. Wang, Z. Wang, C. Zhang, X. Ren, S. Priya, D. Yang, S.F. Liu, Angew Chem. Int. Ed. Engl., (2020) 4238-4244.

[46] A. Dahal, R. Addou, H. Coy-Diaz, J. Lallo, M. Batzill, APL Materials, 1 (2013) 042107, 1-6.

[47] C. Lohaus, (2019), 1-259.

[48] D. Luo, W. Yang, Z. Wang, A. Sadhanala, Q. Hu, R. Su, R. Shivanna, G.F. Trindade, J.F. Watts, Z. Xu, T. Liu, K. Chen, F. Ye, P. Wu, L. Zhao, J. Wu, Y. Tu, Y. Zhang, X. Yang, W. Zhang, R.H. Friend, Q. Gong, H.J. Snaith, R. Zhu, Science, 360 (2018) 1442-1446.

[49] M. Maiberg, T. Hölscher, S. Zahedi-Azad, R. Scheer, J. Appl. Phys., 118 (2015) 105701, 1-10.

[50] S. Yang, J. Dai, Z. Yu, Y. Shao, Y. Zhou, X. Xiao, X.C. Zeng, J. Huang, J. Am. Chem. Soc., 141 (2019) 5781-5787.

[51] S. Song, S.J. Yang, W. Choi, H. Lee, W. Sung, C. Park, K. Cho, Adv. Energy Mater., 10 (2020) 2001759, 1-10.

[52] T. Niu, J. Lu, X. Jia, Z. Xu, M.C. Tang, D. Barrit, N. Yuan, J. Ding, X. Zhang, Y. Fan, T. Luo, Y. Zhang, D.M. Smilgies, Z. Liu, A. Amassian, S. Jin, K. Zhao, S. Liu, Nano Lett, 19 (2019) 7181-7190.

[53] D.-Y. Son, J.-W. Lee, Y.J. Choi, I.-H. Jang, S. Lee, P.J. Yoo, H. Shin, N. Ahn, M. Choi, D. Kim, N.-G. Park, Nat. Energy, 1 (2016), 1-8.

[54] Y. Hou, S. Scheiner, X. Tang, N. Gasparini, M. Richter, N. Li, P. Schweizer, S. Chen, H. Chen, C.O.R. Quiroz, X. Du, G.J. Matt, A. Osvet, E. Spiecker, R.H. Fink, A. Hirsch, M. Halik, C.J. Brabec, Adv. Mater. Interfaces, 4 (2017) 1700007, 1-9.

[55] G. Xu, R. Xue, W. Chen, J. Zhang, M. Zhang, H. Chen, C. Cui, H. Li, Y. Li, Y. Li, Adv. Energy Mater., 8 (2018) 1703054, 1-12.

[56] H. Chen, Y. Zhan, G. Xu, W. Chen, S. Wang, M. Zhang, Y. Li, Y. Li, Adv. Funct. Mater., 30 (2020) 2001788, 1-11.

[57] C. Wang, C. Li, R.C.I. MacKenzie, S. Wen, Y. Liu, P. Ma, G. Wang, W. Tian, S. Ruan, J. Mater. Chem. A, 6 (2018) 17662-17670.

[58] T. Bu, J. Li, F. Zheng, W. Chen, X. Wen, Z. Ku, Y. Peng, J. Zhong, Y.B. Cheng, F. Huang, Nat Commun, 9 (2018) 4609, 1-10.

[59] C. Wang, C. Li, S. Wen, P. Ma, Y. Liu, R.C.I. MacKenzie, W. Tian, S. Ruan, J. Mater. Chem. A, 5 (2017) 3995-4002.

Graphical abstract

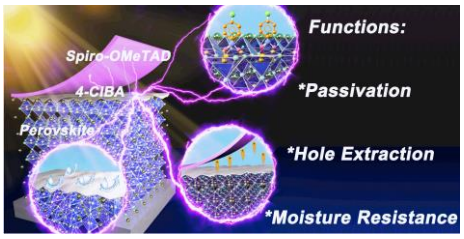

4-ClBA SAM modifier for perovskite/Spiro-OMeTAD interface boosts the device performance, integrating multiple functions of defect passivation, energy level alignment tailoring and moisture resistance.